Performance and stability of Aemion and Aemion+ membranes in zero-gap CO_2 electrolyzers with mild anolyte solutions

Mardle, Peter; Gangrade, Apurva; Saatkamp, Torben; Jiang, Zhengming; Cassegrain, Simon; Zhao, Nana; Shi, Zhiqing; Holdcroft, Steven

Publisher's version / Version de l'éditeur:
https://doi.org/10.1002/cssc.202202376
ChemSusChem, 16, 14, 2023-03-30

ChemSusChem

Research Article
doi.org/10.1002/cssc.202202376

Chemistry Europe
European Chemical Societies Publishing

www.chemsuschem.org

Performance and Stability of Aemion and Aemion+ Membranes in Zero-Gap CO_2 Electrolyzers with Mild Anolyte Solutions

Peter Mardle,[a, b] Apurva Gangrade,[b] Torben Saatkamp,[b] Zhengming Jiang,[a] Simon Cassegrain,[b] Nana Zhao,[a] Zhiqing Shi,*[a] and Steven Holdcroft*[b]

The dependence of performance and stability of a zero-gap CO_2 electrolyzer on the properties of the anion exchange membrane (AEM) is examined. This work firstly assesses the influence of the anolyte when using an Aemion membrane and then shows that when using 10 mM $KHCO_3$, a CO_2 electrolyzer using a next-generation Aemion+ membrane can achieve lower cell voltages and longer lifetimes due to increased water permeation. The impact of lower permselectivity of Aemion+ on water transport is also discussed. Using Aemion+, a cell voltage of 3.17 V at 200 mA cm^{-2} is achieved at room temperature, with a faradaic efficiency of >90%. Stable CO_2 electrolysis at 100 mA cm^{-2} is demonstrated for 100 h, but with reduced lifetime at 300 mA cm^{-2}. However, the lifetime of the cell at high current densities is shown to be increased by improving water transport characteristics of the AEM and reducing dimensional swelling, as well as by improving cathode design to reduce localized dehydration of the membrane.

Introduction

In recent years, the rapid development of anion exchange membranes (AEMs) has led to significant advances in electrochemical conversion systems such as redox flow batteries,[1,2] fuel cells,[3–5] water electrolyzers,[6–9] and CO_2 electrolyzers.[10,11] Many of these devices benefit from the alkalinity that the fixed positively charged functional groups of the solid polymer electrolyte can provide. For example, cheaper and more abundant non-noble metal catalysts can be more readily utilized with reduced corrosion under caustic conditions.[12–14] High pH also favors the kinetics of some electrochemical reactions such as the oxygen evolution reaction (OER),[15] and in the particular case of CO_2 reduction (CO_2R), inhibits parasitic hydrogen evolution reaction (HER).[16] For example, Durst *et al.*, found that the exchange current density for hydrogen evolution/oxidation reactions is two orders of magnitude lower at pH 13, compared to pH 0 on carbon supported noble metal catalysts.[17] The result of this inhibition is much greater faradaic efficiencies (FEs) for CO_2 electrolyzers utilizing an AEM over a cation exchange membrane (CEM),[18] although novel cell design may address this challenge for CEMs.[19]

With high FEs, low temperature CO_2 electrolyzers are approaching economic viability for a variety of product materials.[20–22] However, several critical issues currently obstruct industrial adoption of these technologies. Firstly, dissolved CO_2 rapidly converts to HCO_3^-/CO_3^{2-} under caustic conditions which can readily migrate and diffuse across the AEM to the anode, owing to AEM's fixed positively charged functional groups.[23,24] When using metal hydroxide electrolytes, carbonation and subsequent carbonate ion crossover leads to rapid neutralization of the electrolyte, resulting in an increase in cell voltage.[25–27] With bicarbonate electrolytes, the pH is maintained by protonation of additional HCO_3^- into H_2CO_3 with subsequent decomposition, wherein CO_2 evolves alongside O_2 at the anode.[28] Both regenerating hydroxide electrolytes and separating anode gases would impart extensive energy costs,[18,29,30] and so alternative systems such as the reduction of carbon monoxide or bipolar membrane electrolysis systems are receiving increased attention.[31–37] Other strategies such as AEM modifications towards reducing carbonate ion crossover, in addition to decreasing the crossover of neutral products have been proposed,[10] yet for any reduction in the migration of CO_3^{2-} species, the charge-transfer rate of CO_2 reduction must first exceed the rapid rate of carbonation.[38]

In addition to carbonate ion crossover, the combined high concentrations of HCO_3^-/CO_3^{2-} and cationic species results in salt precipitation at the cathode and blockage of the flow field channels.[39] This leads to a reduction in the mass flow of CO_2 reactants, a subsequent loss of FE for CO_2R and eventually cell failure. Strategies to circumvent this include periodic water purging to remove salts in the electrode and flow field channels,[40–42] intermittent electrolysis at low current densities

[a] Dr. P. Mardle, Z. Jiang, Dr. N. Zhao, Dr. Z. Shi
Energy, Mining & Environment Research Centre
National Research Council Canada
Vancouver, BC V6T 1 W5 (Canada)
E-mail: zhiqing.shi@nrc-cnrc.gc.ca
[b] Dr. P. Mardle, A. Gangrade, Dr. T. Saatkamp, Dr. S. Cassegrain, Prof. S. Holdcroft
Department of Chemistry
Simon Fraser University
Burnaby, BC V5 A 1S6 (Canada)
E-mail: holdcrof@sfu.ca

Supporting information for this article is available on the WWW under https://doi.org/10.1002/cssc.202202376

to allow CO_3^{2-} migration to exceed the rate of generation,[43] and using pure water at the anode to avoid salt precipitation altogether.[44] All three methods entail specific disadvantages: Purging the cathode flow field can exacerbate the flooding of the gas diffusion layer, inhibiting CO_2 mass transport, in addition to removing all of the cationic species, which are pivotal in the activation of many CO_2R electrocatalysts.[26,45] Hence, when using pure water as the electrolyte, cationic species need to be introduced into the cathode by flushing with electrolyte, for example.[44] Voltage fluctuations from intermittent electrolysis may also exacerbate catalyst degradation, although start-stop degradation tests need to be developed and conducted for different CO_2R electrocatalysts.[46] The cumulative loss of operational time would need to be considered in the technoeconomic analysis of such systems. Nevertheless, Samu *et al.*,[47] demonstrated excellent system stability for CO_2R to CO under dynamic operation, as did Xu *et al.*,[43] in their implementation of a self-cleaning protocol.

Despite these challenges, there has been great success in achieving efficient CO_2 electrolysis (CO_2E) systems with AEMs. For example, Endrödi *et al.*, achieved a partial current density of CO (I_{CO}), over 1 A cm^{-2}, when utilizing a 15 μm, PiperION AEM reinforced with PTFE.[48] Significant system stability was also demonstrated with both 0.01 and 0.1 M CsOH anolytes, where hydration of the CO_2 feed gas was shown to be critically important. With such advances, we sought to further elucidate how specific AEM properties influence the cell voltage, FE, and durability of low temperature CO_2E systems.

Here, the differences in performance between two anolyte systems (1 M KOH reported previously,[26] and 10 mM $KHCO_3$) are compared, followed by an experimental investigation on how various properties of polybenzimidazolium- and polyimidazolium-based AEMs, distributed under the brand name Aemion and Aemion+, affect the performance of CO_2E with low concentration $KHCO_3$ anolytes operating at room temperature. The stability of the electrolyzer at a current density of 300 mA cm^{-2} is finally studied, correlating AEM design with various degradation phenomena. This work has the objective of providing an enhanced understanding of what constitutes an effective AEM for CO_2E applications, as well as highlighting the confluence of transport phenomena that impact the final performance and stability of these systems.

Results and Discussion

1 M KOH and 10 mM $KHCO_3$ anolytes

The influence of the electrolyte on the electrochemical reduction of CO_2 has been extensively studied in flow reactors where the solution is in intimate contact with the electrocatalyst. For example, Verma *et al.*, demonstrated lower CO_2R overpotentials with higher cation concentrations, and higher pH electrolytes, for example, KOH < $KHCO_3$ < KCl.[49] The mechanism of cation activation of the CO_2R has also been studied,[50] with the overpotentials for CO_2R typically following the order $Cs^+ < K^+ < Na^+ < Li^+$, owing to a smaller hydration radius increasing the surface charge density at the catalyst surface.[51] For zero-gap electrolyzers, only an anolyte is typically used and so the anode is analogous to that of an AEM water electrolyzer (AEM-WE). For the AEM-WE, it has been shown that an increase in the anode pH and electrolyte conductivity enlarges the active surface area of the catalyst, improves OER kinetics and reduces the ionic transport resistance in the catalyst layer.[52]

Figure 1a shows the difference in IV performance between two extremes; the best performing cell developed in our previous work with 1 M KOH anolyte,[26] and the cell used for this study with 10 mM $KHCO_3$ anolyte. A schematic illustration of the electrolysis system is shown in Figure S1. Aemion of thickness 25 μm (AF1-HNN8-25-X) was used for both tests. Despite the higher catalyst loading and utilization of IrO_x catalyst in the commercial electrodes, changing the anolyte to 10 mM $KHCO_3$ led to an increase in overpotential of 817 mV at 100 mA cm^{-2}. Assuming a Nernst potential of 1.34 V,[53] this constitutes a 15 % drop in the voltage efficiency, from 58 % with 1 M KOH to 43 % with 10 mM $KHCO_3$. It is also noted that over triplicate tests, the standard deviation for the 10 mM $KHCO_3$ anolyte (0.11 V) is higher than the 1 M KOH anolyte (0.01 V) at 100 mA cm^{-2}. In efforts to mitigate this variance in voltage when using 10 mM $KHCO_3$ anolytes, the cell was activated at high current density prior to acquisition of *IV* curves.

Nyquist plots from electrochemical impedance spectroscopy (EIS) at 25 mA cm^{-2} are shown in Figure 1b. The high frequency resistance of the cell – extracted from equivalent circuit modelling (Figure S2 in the Supporting Information) – was significantly higher for the 10 mM $KHCO_3$ system at 1.31 ± 0.10 Ω cm^2, compared to 0.41 ± 0.01 Ω cm^2 for the previously reported cell. This is likely due to a much reduced conductivity of the anolyte (1.1 mS cm^{-1} for 10 mM $KHCO_3$,[54] compared to 215 mS cm^{-1} for 1 M KOH)[55] and expected lower conductivity of the AEM. For example, the conductivity of Aemion in the hydroxide form was measured to be 103 mS cm^{-1} (40 °C, 90 % relative humidity (RH)) compared to around 15 mS cm^{-1} in the mixed HCO_3^-/CO_3^{2-} form.[56] Additionally, the total charge transfer resistance for the 10 mM $KHCO_3$ system is higher at 13.86 ± 2.73 Ω cm^2 compared to 6.04 ± 0.08 Ω cm^2 for the 1 M KOH system. Two resistance features are visible in both the Nyquist and the Bode plots (Figure S4) for the 10 mM $KHCO_3$ system. Differentiating these two features is discussed in the next section, however comparisons cannot be made with the 1 M KOH since these resistance elements are too convoluted to be reliably separated through equivalent circuit modelling.

In order to investigate the influence of cation concentration, a 1 M $KHCO_3$ anolyte was also examined. Figure S5a shows similar *IV* performances for Aemion operating with 10 mM $KHCO_3$ and 1 M $KHCO_3$ anolytes although the higher concentration resulted in a reduced high frequency resistance of 0.86 ± 0.15 Ω cm^2 and total charge transfer resistance of 7.12 ± 0.34 Ω cm^2 at 25 mA cm^{-2} (Figure S5c). Discrepancy from the final cell voltage (E_{Cell}) suggests that with different concentration of bicarbonate electrolytes, there are differences in the thermodynamic potential of the cell due to differences in OH^- concentration between the anode and cathode. For example,

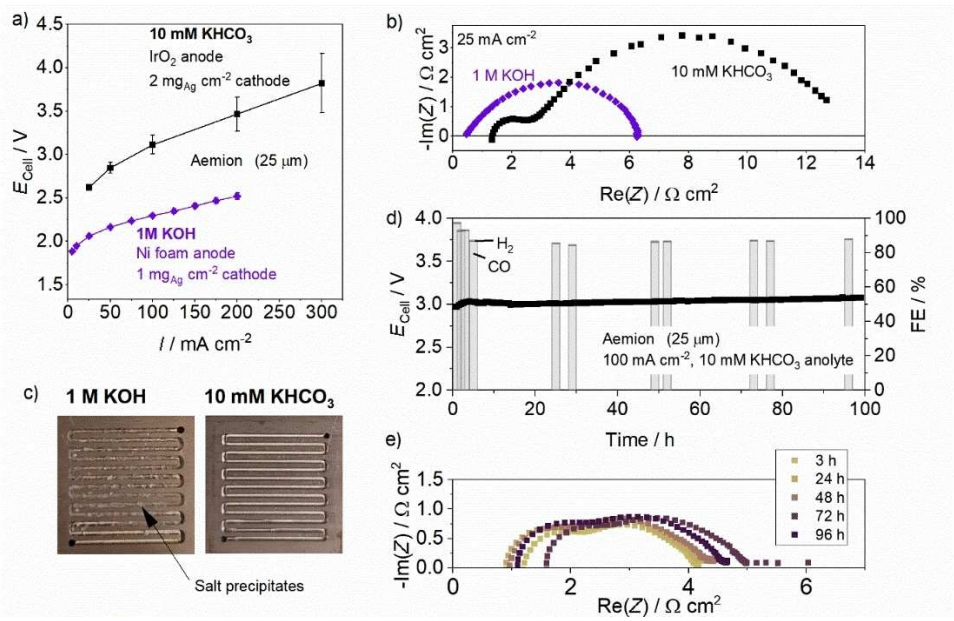

Figure 1. a) *IV* curves obtained for 5 cm^2 CO_2E cells at room temperature utilizing an Aemion (AF1-HNN8-25-X) membrane in the 1 M KOH system and 10 mM $KHCO_3$ anolyte system. Data for the 1 M KOH anolyte system are reproduced from Ref. [26] with permission from the American Chemical Society, Copyright 2021. 1 M KOH was supplied at a rate of 10 mL min^{-1} (single pass). A Ni foam anode and Ag/C (95 wt% Ag) cathode of loading 1 mg_{Ag} cm^{-2}, with 30 wt% PTFE binder were used. Dry CO_2 was supplied at a rate of 100 mL min^{-1}. For the 10 mM $KHCO_3$ anolyte, 500 mL was recirculated at a rate of 10 mL min^{-1}. Ag cathode and IrO_2 anodes (Dioxide Materials) were used. All electrodes cut to exactly 5 cm^2. Humidified CO_2 was supplied to the cathode at a rate of 30 mL min^{-1}. b) Nyquist plots at 25 mA cm^{-2} in the frequency range 10 kHz to 0.1 Hz. c) Differences in salt precipitation after *IV* curve acquisition in 1 M KOH and after 100 h of operation at 100 mA cm^{-2} with 10 mM $KHCO_3$ anolytes. d) E_{Cell} (symbols) and FE (bars) of the cathode gases during 100 h of operating the 10 mM $KHCO_3$ anolyte system at 100 mA cm^{-2}. e) EIS during the 100 h experiment in the frequency range 10 kHz to 0.1 Hz.

an increase in the pH at the cathode with respect to the anode (by virtue of a higher K_2CO_3 concentration with more concentrated $KHCO_3$ anolytes) would result in an increase in the thermodynamic voltage of the full cell, which does not directly contribute to the impedance response. For KOH anolytes, a high pH at the anode results in a smaller thermodynamic overpotential,[38] which alongside reduced ohmic resistance and increased electrode kinetics results in an enhancement of performance when using mild anolytes. However, a higher concentration of K^+ leads to a reduction in the faradaic efficiency of CO production (FE_{CO}) due to an increase in the electro-osmotic drag of water, exacerbating flooding of the cathode and resulting in increased mass transport limitations for CO_2R.[26] Figure S5b shows that for the same cathode (Dioxide Materials), FE_{CO} was significantly lower for the higher concentration of K^+ (29% for 1 M $KHCO_3$ and 85% for 10 mM $KHCO_3$, at 300 mA cm^{-2}). For this reason, the 1 M KOH system utilized a PTFE in the cathode catalyst layer to promote reverse transport of water through the membrane.[57]

Critical differences concerning real world applicability also arises when comparing the stability of the 1 M KOH and 10 mM $KHCO_3$ systems. For example, utilization of the 1 M KOH system leads to neutralization of the anolyte as well as significant salt precipitation, resulting in cell failure without water purging steps.[26] Figure 1c shows that, in contrast to using 1 M KOH anolytes, use of 10 mM $KHCO_3$ results in little salt precipitation at the cathode after 100 h of continuous operation at a current density of 100 mA cm^{-2}. Figure 1d shows the cell voltage and FE of the electrolyzer during this test, which is comparable to a reference Sustainion X37-50 Grade RT membrane shown in Figure S6. In depth comparisons with other commercial membranes are beyond the scope of this study. For Aemion, the voltage rose by +0.9 mV h^{-1} in the linear region of 15–100 h. EIS analysis shown in Figure 1e indicates that this rise in voltage is due to increases in high frequency resistance (HFR) and potential degradation of the membrane. The FE of CO formation was also consistently high at 86% for most of the experiment. Deviation from the initial FE of 97% is likely due to mechanical stress on the AEM during electrolysis under these conditions, which as discussed in subsequent sections is an additional result of membrane dehydration. Considering the high stability and the reduced propensity for cathode flooding of the 10 mM $KHCO_3$ system over that using 1 M KOH, we sought to further understand how AEM properties affect both the performance and stability of zero-gap CO_2 electrolyzers operating with mild anolyte solutions.

IV characteristics of Aemion and Aemion+ for CO_2E

To probe the effects that AEM properties have on the performance and stability of CO_2 electrolyzers utilizing mild $KHCO_3$ anolyte, Aemion and Aemion+ materials were examined. These have been extensively characterized in a previous publication and salient properties in the Cl^- counterion form are resummarized in Figure 2a.[58] The primary difference between

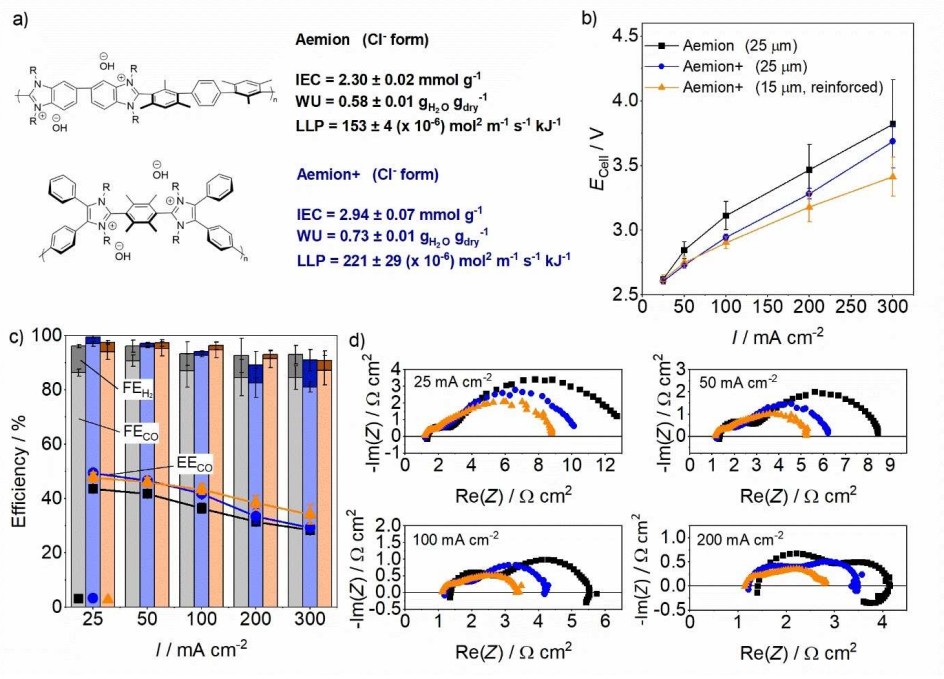

Figure 2. a) Cationic functional group structures and ex situ characterization of Aemion and Aemion+ (non-reinforced) in the Cl^- form. Full polymer structures are proprietary information of Ionomr Innovations Inc. Water uptake (WU) was measured at room temperature whereas the liquid-liquid permeability (LLP) was measured at 70 °C. Data were obtained from Ref. [62] with permission from the Royal Society of Chemistry. Copyright 2022. b) *IV* curves for a 5 cm^2 CO_2E cell operating with different AEMs (AF1-HNN8-25-X, AH2-INN8-25-X, AF2-CLE8-15-X) at room temperature with 10 mM $KHCO_3$ anolyte (500 mL) recirculating at 10 mL min^{-1}. Humidified CO_2 was supplied to the cathode with a flow rate of 30 mL min^{-1}. Ag cathode and IrO_2 anodes (Dioxide Materials) were cut to exactly 5 cm^2. c) Faradaic efficiency (FE) of the cathode gases and the calculated energetic efficiency (EE) for each AEM at the tested current densities. d) Representative Nyquist plots obtained in the frequency range 10 kHz to 0.1 Hz.

these materials lies in the cationic functionality, the former being benzimidazolium; the latter, imidazolium, which has been demonstrated to possess significantly higher chemical stability towards hydroxide-ions. Aemion+ has similar ionic conductivity but higher water permeability compared to Aemion, noted as a critical factor for the stable operation of a CO_2 electrolyzer.[39]

When utilizing 10 mM $KHCO_3$, significant differences in electrolyzer performance were observed when changing the AEM to Aemion+. Figure 2b shows that in the current density range of 100–300 mA cm^{-2}, Aemion+ of equal thickness to Aemion exhibits an lower average E_{Cell} of around 160 mV. At 200 mA cm^{-2}; $E_{Cell} = 3.47 \pm 0.19$ V for Aemion and 3.28 ± 0.04 V for Aemion+. The average FE_{CO} was also measured to be slightly higher, as shown in Figure 2c, although this is within error of the measurement. For all AEMs, the FE_{CO} was above 80% in all current densities, although at higher current density, the total FE of all gases drops to around 90%, which may indicate increases in product crossover. The stability of each material to gas and carbonate ion crossover was beyond the scope of this current study, but is part of separate, detailed study. A thinner variant of Aemion+ was also investigated. Without reinforcement, cells comprising 10 μm Aemion+ immediately failed upon application of a current density of 300 mA cm^{-2}. More stable operation was attained by the use of a polyolefin reinforcement, in addition to the slightly thicker AEM of 15 μm. The thinner, reinforced Aemion+ exhibited similar voltages to the 25 μm Aemion+ membrane at low current densities, but enhanced performance at 200 mA cm^{-2} ($E_{Cell} = 3.17 \pm 0.11$ V vs. 3.28 ± 0.04 V) and 300 mA cm^{-2} ($E_{Cell} = 3.41 \pm 0.15$ V vs. 3.69 ± 0.12 V). Such differences in voltage for these membranes is contrary to CO_2E utilizing 1 M KOH anolyte, where similar performances were observed for both 15 μm reinforced Aemion+ and 25 μm Aemion membranes. Figure S7 shows that when using 1 M KOH, the *IV* curves gave very similar voltages (at 200 mA cm^{-2}; 2.52 ± 0.04 V for Aemion and 2.60 ± 0.02 V for Aemion+) while the FE for CO was slightly lower for Aemion+ in comparison to Aemion.

To better understand the root cause of these performance enhancements, EIS analysis was conducted. Representative Nyquist plots between 25–200 mA cm^{-2} are shown in Figure 2d. Equivalent circuit modelling was conducted using the circuit depicted in Figure S2, with resultant data shown for each AEM in Figure S8. The HFR for all membranes was measured to be in the range 1.0–1.5 Ω cm^2 which as previously mentioned is likely a product of the low conductivity of the anolyte solution. Nevertheless, the HFR follows the order of Aemion+ (15 μm, reinforced) < Aemion+ (25 μm) < Aemion (25 μm). Considering similar trends in ionic conductivity measured ex situ, changes in the HFR could also indicate changes in the hydration of the AEM and thus differences in conductance under operating conditions.

Figure 2d shows that more significant differences in the Nyquist plots between the AEMs were measured with the low frequency resistance elements, which are typically attributed to

charge transfer and mass transport resistances. As shown by the Nyquist plots in Figure 2d, there are generally two resistance features. Bode plots shown in Figure S9, indicate that the peaks of these features occur at around 2000 Hz and 10 Hz. Equivalent circuit modelling in Figure S8 shows that for all AEMs, the low frequency feature dominates at low current densities, but decreases significantly with increasing current density, suggesting that a significant portion is related to charge transfer resistances. On the other hand, the HFR and the resistance feature at 2000 Hz remain comparatively constant at all current densities. This might suggest an ohmic-type resistance associated with the higher resistance element. Considering that the CO_2R and OER reactions are considered to have similar overpotentials,[38] it is likely that the anode and cathode charge transfer elements are convoluted in the low frequency resistance feature. Evidence of this might be found with the EIS response of the reinforced Aemion+, which exhibited the lowest overall resistance. Bode plots (Figure S9) show that for the reinforced membrane, the low frequency element splits into two separate features with characteristic frequencies of 20 Hz and 100 Hz. Fully decoupling the resistance features would be greatly assisted by the use of an external reference electrode, with recent designs showing promise.[59,60] However considering that the OER conditions are identical for each AEM, it can be concluded that the AEM properties are not just affecting the ohmic losses associated with ionic conductivity, but also have a direct influence on the electrocatalytic performance of the cathode.

AEM permselectivity

Referring to earlier mentioned studies concerning the enhancement of CO_2R by adsorbed alkali metal cations, we considered that the performance characteristics of AEMs in CO_2 electrolyzers may be related to the co-ion leakage of cations from the anolyte to the cathode where it can activate the CO_2 reduction reaction.[51] Previous work by Gangrade *et al.*,[61] demonstrated the selectivity of Cl^- transport from NaCl solutions through Aemion follows a linear relation with the fixed charge group concentration (c_{FCG}. Permselectivity was measured by the static method, based on the measurement of the membrane potential that develops across an ion exchange membrane (IEM) when it is separated by two electrolytes of same composition, but different concentration (Figure 3a, b).

Data from our previous work is reproduced within Figure 3 for Aemion,[61] wherein additional measurements on Aemion+ AEMs are added for this study. Even though permselectivity measurements for $KHCO_3$ solutions are more applicable for the environment of the CO_2 electrolyzer, other factors influence

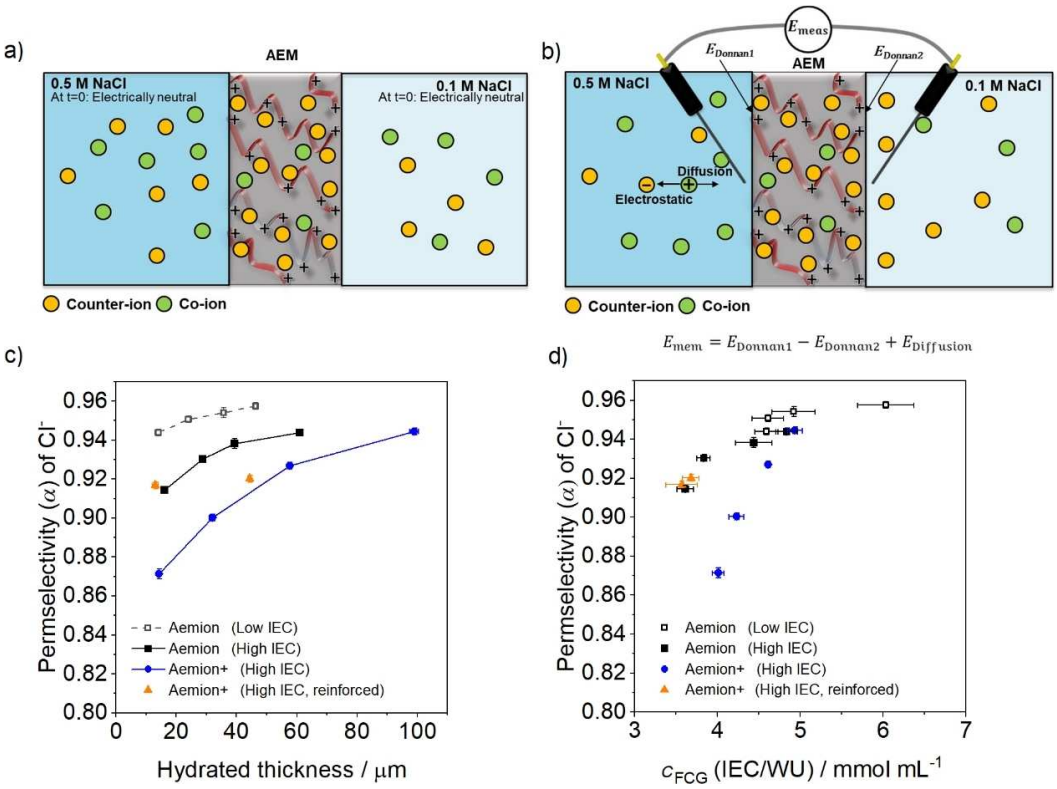

Figure 3. Schematics showing how membrane potential (E_{meas}) forms for the static method for measuring the permselectivity of AEMs. a) AEM pre-equilibrated in 0.5 M for 48 h, separating 0.5 M and 0.1 M NaCl solutions b) Membrane potential measured using Ag/AgCl wire reference electrodes. Using the stablized membrane potential values, the permselectivity for Cl^- ions in NaCl solutions measured at room temperature of 20±0.3 °C, is shown for the different AEMs; AF1-HNN5-X (low IEC), AF1-HNN8-X (high IEC), AH2-INN8-X (high IEC) and AF2-HLE8-X (high IEC, reinforced) vs. c) the hydrated thickness and d) Fixed charge group concentration (c_{FCG}). Data for Aemion is reproduced from Ref.[49] with permission from Elsevier. Copyright 2022.

permselectivity of the membrane under operational conditions. This includes water flux by electro-osmotic drag, hydraulic permeation and the nature of the counterion in the membrane ($OH^-/CO_3^{2-}/HCO_3^-$), all dependant on the current density.[38] To critically asses the intrinsic properties on the membrane absent of these factors, and to serve as a reference data set for future studies on Aemion+ membranes, permselectivity measurements were limited to NaCl solutions, although we reasonably anticipate similar trends between the AEMs for $KHCO_3$ solutions and during electrolyzer operation.[62]

A key trend observed in these measurements, and illustrated in Figure 3c, is an increase in the permselectivity for thicker AEMs due to the relatively lower water uptake of thicker AEMs with similar ion exchange capacity (IEC, Table S1). For example, while Aemion+ exhibited a water uptake of $0.73 \pm 0.01\ g_{H_2O}\ g_{dry}^{-1}$ (0.1 M NaCl) for the membranes of wet thickness 14 ± 1 μm, this was reduced to $0.60 \pm 0.01\ g_{H_2O}\ g_{dry}^{-1}$ for the membranes of wet thickness 99 ± 1 μm. The lower water uptake with increased membrane thickness results in an increased c_{FCG} which in turn enhances the co-ion exclusion according to the Donnan exclusion principle.[61] As a result, the permselectivity for the thickest Aemion+, measured to be 0.944 ± 0.002, reduced to 0.871 ± 0.003 for the thinnest membrane. While Aemion+ possessed a similar c_{FCG} in comparison to the first generation Aemion materials, Figure 3d shows that the permselectivity is lower than expected from the linear relation measured for Aemion with different IECs. This is related to differences in the diffusion potential ($E_{Diffusion}$) arising from higher water volume fraction in Aemion+ (Table S1). $\frac{D_i^{mem}}{D_i^{solution}} = \left(\frac{\varphi_w}{2-\varphi_w}\right)^2$. φ_w is the water volume fraction in the membrane, D_i^{mem} and $D_i^{solution}$ are the diffusion coefficients of an ion in the membrane and in the solution, respectively. The higher water volume fraction in AEMs causes increased salt diffusion and hence increased co-ion diffusion, resulting in reduced permselectivity.[61–63] Two Aemion+ membranes containing reinforcement were also measured. While the hydration of the ions was previously found to be equivalent for the non-reinforced and reinforced materials,[58] the liquid water permeability was lower with reinforcement, and similar to Aemion. As a result, a similar permselectivity of 0.92 was obtained, matching the linear trend of permselectivity vs. c_{FCG} for Aemion membranes, as shown in Figure 3c.

By comparing the permselectivity data and hydraulic water permeability with Figure 2b, it is found that smaller low frequency resistances and lower E_{Cell} for Aemion+ over Aemion AEMs in CO_2E electrolysis can be directly attributed to reduced permselectivity and higher water permeability. It is noted that cationic enhancement of CO_2R is a surface phenomenon, independent of the concentration in the diffuse layer.[51] Therefore, provided that there are sufficient cations to activate the electrochemically active surface area (ensured by the cell break-in procedure) the increased flux of cations towards the cathode via co-ion leakage through a less permselective AEM should not influence the kinetics of CO_2R. Rather, a higher co-ion leakage will result in an increase in the electro-osmotic drag of water from the anolyte. It is hypothesized that this increase in water flux alleviates mass transport limitations under these test conditions which are shown in the following sections to also be a significant factor in the stability of this system. Although the thinner, reinforced Aemion+ exhibited similar permselectivity and water permeability to Aemion, the improved performances are likely due to increases in water flux by virtue of higher water chemical potential gradients and higher electrical potential gradients. It is reiterated that these performance enhancements were only found for low concentration anolytes and so water flux by co-ion leakage appears to be a significant factor in the overall hydration of the cathode, in addition to water diffusion and hydraulic permeation.

Stability of AEMs for CO_2E at room temperature

Figure 1d shows that for the Aemion membrane, high CO_2R efficiency was maintained for 100 h of continuous operation. This was also observed for the best performing Aemion+ AEM (15 μm, reinforced) as shown in Figure 4a, highlighting that both membranes can provide stable CO_2E for at least 100 h. The FE of the reinforced AEM was also sustained for longer, ranging from 92–97% with a voltage increase of $0.5\ mV\,h^{-1}$ in the timeframe of 15–100 h. For the 15 μm reinforced Aemion+ membrane the impedance response shown in Figure 4b exhibited negligible changes after the initial rise in voltage, coinciding with an increase in the low frequency resistance. This is contrary to the Aemion membrane where Figure 1e shows an increase in HFR. Nuclear magnetic resonance spectroscopy (NMR) of both AEMs is shown in Figure S10, where no chemical degradation was observed.

To better examine how AEM properties influence their stability in CO_2 electrolyzers, we sought to examine degradation behaviour at a high enough current density to accelerate cell failure. While this forgoes the benefits of quantitative analyses, this strategy was found to be more informative for future AEM design. Figure 4c shows the cell voltage for the three primary AEMs of interest (Aemion and the two Aemion+ membranes), operating at a current density of $300\ mA\,cm^{-2}$, at room temperature. It was found that at these high applied current densities, the cell voltage for Aemion started to increase exponentially, hitting the set cap of 5 V after 1.5 h. Aemion+ of same, 25 μm, thickness started to follow the same trend although at a slower rate.

Similar CO_2 electrolyzer degradation to that observed in this study has been reported in the literature. Liu *et al.,* noted that cell voltage increases were dependent on the current density, with shorter lifetimes at higher cell voltages.[64] They concluded that this was due to dehydration at the cathode, alleviated through the use of $KHCO_3$ anolyte over DI water to encourage electro-osmotic drag through co-ion leakage. This observation is contrary to reports utilizing >10 mM electrolytes where flooding of the cathode is typically observed due to too high bulk water transport.[57,65] Flooding in zero-gap configurations should not be confused with reports on flow-cell CO_2 electrolyzers where flooding greatly depends on the interface between the gas diffusion electrode (GDE) and the catholyte rather than

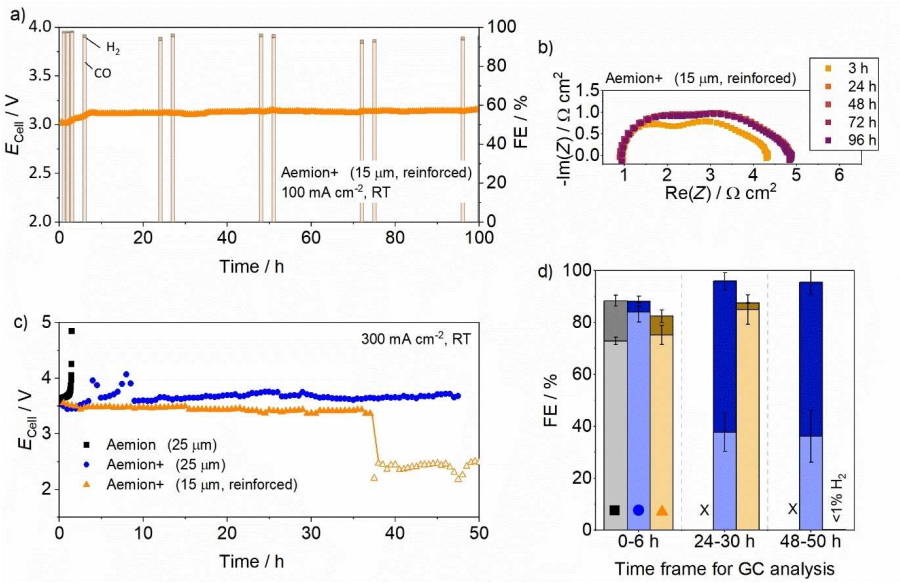

Figure 4. a) E_{Cell} (symbols) and FE (bars) of the cathode gases during 100 h of operating a membrane of Aemion+ (AF2-CLE8-15-X, 15 µm, reinforced) in a 5 cm^2 CO_2E cell (100 mA cm^{-2}, room temperature). b) Representative Nyquist plots obtained in the frequency range 10 kHz to 0.1 Hz for Aemion+ (15 µm, reinforced) at 100 mA cm^{-2}. c) E_{Cell} obtained at the current density of 300 mA cm^{-2} using different AEMs (AF1-HNN8-25-X, AH2-INN8-25-X, AF2-CLE8-15-X. d) Average FE for the cathode gases during 3 time periods. The symbols identify the AEMs from the legend of (c). "X" signifies that there was negligible detection of H_2 or CO.). For all tests, 10 mM $KHCO_3$ anolyte (500 mL) was recirculated at 10 mL min^{-1}. Humidified CO_2 was supplied to the cathode with a flow rate of 30 mL min^{-1}. Ag cathode and IrO_2 anodes (Dioxide Materials) were cut to exactly 5 cm^2.

transport phenomena through the membrane.[66–68] Here, water transport to the cathode is a combination of water permeation and electro-osmotic drag through the mechanism of co-ion leakage. As previously discussed, Aemion has lower water permeability in comparison to Aemion+ and also has a higher permselectivity towards anions, which would likely result in reduced co-ion leakage and thus less water flux towards the cathode. It can be reasonably suggested that this is the underlying cause for the differences between the stability of Aemion and Aemion+. This also agrees with the observed HFR increase – indicated by the EIS spectra at 100 mA cm^{-2} (Figure 1e and Figure 4b) – which could be the result of dehydration of the AEM and loss of conductivity at the cathode-membrane interface, exacerbated at higher current densities.

After 4 h of electrolysis, the voltage of the Aemion+ suddenly drops, followed by a further increase until 8 h. After 8 h, the voltage remained stable, however, as shown in Figure 4d, the FE for H_2 greatly increased to around 58% and remained stable thereafter. Upon disassembly, critical weakening of the edges of the AEM was observed (shown in Figure S11) and so it is thought that edge failure resulted in direct anolyte flow to the cathode side causing critical flooding of the gas diffusion and catalyst layers which induced mass transport limitations for CO_2R.

To investigate the cause of edge failure, dimensional swelling of the AEMs was examined. While ex situ characterization is conventionally performed in the Cl^- form, the HCO_3^- form was chosen for this study to examine the AEM properties more closely related to the CO_2E system, while avoiding difficulties in the mixed OH^-/CO_3^{2-} form under exposure to air. Table 1 shows that water uptake was higher for Aemion+ (1.53±0.10 g_{H_2O} g_{dry}^{-1}) compared to Aemion (1.32±0.03 g $_{H_2O}$ g_{dry}^{-1}) and significantly higher than in the Cl^- form (Figure 2a). As a result, dimensional swelling in the HCO_3^- form was high, at 92±3% for Aemion and 152±1% for Aemion+.

Table 1. Salient and mechanical properties for Aemion and Aemion+ in the HCO_3^- counterion form. All measurements were recorded under ambient conditions (20 °C, 30–35 %RH). S_{xyz} corresponds to the dimensional swelling of the membranes. S_{xy} and S_z are the swelling of the membrane area (xy-plane) and thickness (z-direction), respectively.

AEM Property (HCO3⁻ form)	Aemion (25 µm)	Aemion+ (25 µm)	Aemion+ (25 µm, reinforced)	Aemion+ (15 µm, reinforced)
WU [g_{H_2O} g_{dry}^{-1}]	1.32±0.03	1.53±0.10	1.44±0.03	1.37±0.04
S_{xyz} [%]	92±3	152±1	98±1	82±3
S_{xy} [%]	61±3	57±1	36±1	33±2
S_z [%]	19±1	60±1	45±1	37±1
tensile Strength [MPa]	31±6	43±10	82±7	124±9
elongation at break [%]	70±25	93±35	128±16	97±12
Youngs modulus [MPa]	1265±95	1300±117	1064±28	1583±336

During CO_2E, the active area of the membrane on the cathode side is expected to be become dehydrated due to water consumption and deleteriously pull away from the hydrated membrane pinched by the gaskets. A larger degree of dimensional swelling (i.e., a larger discrepancy in membrane dimensions in the wet and dry state) results in more significant stress at the edge of the membrane,[69] and thus a higher propensity for edge failure.

A strategy to reduce dimensional swelling and to increase AEMs mechanical robustness is the inclusion of a porous reinforcement. With an equal dry thickness of 25 μm, the dimensional swelling of Aemion+ in the HCO_3^- form in water was reduced from 152±1% to 98±1% by the introduction of a polyolefin-based reinforcement. With the thinner, 15 μm membrane, the dimensional swelling was reduced further to 82±3%. An added benefit of the reinforcement is the much-increased tensile strengths of 82±7 MPa and 124±9 MPa for the 25 μm and 15 μm reinforced Aemion+ under ambient conditions (20 °C, 30–35% RH) respectively, in comparison to 43±10 MPa for the non-reinforced Aemion+. Compared to AEMs in their halide form, AEMs in the HCO_3^- form were found to have lower tensile strength under ambient conditions. For example, while the tensile strength for Aemion was previously measured to be 51±8 MPa for Aemion in the Cl^- form,[58] it was found to be 31±6 MPa in the HCO_3^- form. These differences mainly arise from the differences in hygroscopicity of the AEMs in different ion forms that causes differences in water content under same (*T*, RH) conditions. AEMs of lower water content typically exhibit more rigid and stiff tensile behavior with higher yield strength and Young's modulus, and commonly, lower elongation at break.

As a result of the increased strength and reduced swelling, Aemion+ (15 μm, reinforced) provided high FE_{CO} and a comparatively stable cell voltage of around 3.44 V until 38 h where the cell voltage dropped by around 1 V (Figure 4d, e). No edge failure was observed in contrast to the non-reinforced Aemion+ of higher thickness, however a pinhole was clearly observed upon disassembly (Figure S12a). A greater difference in the EIS spectra was also observed after pinhole formation, where Figure S13 shows a large increase in both HFR and CT resistances, unlike Aemion+ where edge failure exhibited less definitive changes in the impedance response. It is noted that post-mortem NMR analysis of the 15 μm Aemion+ showed no indication of defunctionalization through reaction with hydroxide species (Figure S12b) as with the lower current density of 100 mA cm^{-2} and so pinhole formation appears to also be mechanical in nature. It is therefore considered that unlike edge failure, which is dependent on large structural changes, thin-reinforced membranes remain susceptible to localized structural changes which can occur due to differences in local current densities.

Stability of CO_2 electrolyzers utilizing Aemion+ at 50 °C

Water permeance through the membranes is expected to increase with temperature,[70] leading to the hypothesis that elevated cell temperatures might alleviate some of the mechanical degradation during CO_2E at high current densities. Higher temperatures also allow for a greater supply of water vapor to the cathode, as well as faster electrode kinetics, and so the stability of various Aemion+ membranes operating at 50 °C was examined.

Figure 5 shows that pinhole formation was still observed at elevated temperature for the 15 μm Aemion+ membrane after 6 h of operation. For the non-reinforced, 25 μm Aemion+, elevated temperature extended the operation at 300 mA cm^{-2} to >100 h, with an average cell voltage of 3.27 V. The FE of the cathode gases was recorded and as shown in Figure 5 was maintained at >90% for the duration of the experiment. After disassembly, the edge of the AEM was found to be intact, unlike the experiment at room temperature where edge failure was observed (Figure S11). It is thought that at a higher operating temperature, edge failure was alleviated due to higher water permeance, maintaining the hydrated structure of the membrane at the edges. However, a gradual decrease in the total FE was observed, although this was within error of the measurement. The voltage also dropped from 40 h at a rate of 0.4 mV h^{-1}, suggesting an increase in gas crossover and parasitic reactions at each electrode. Coinciding with this, EIS analysis

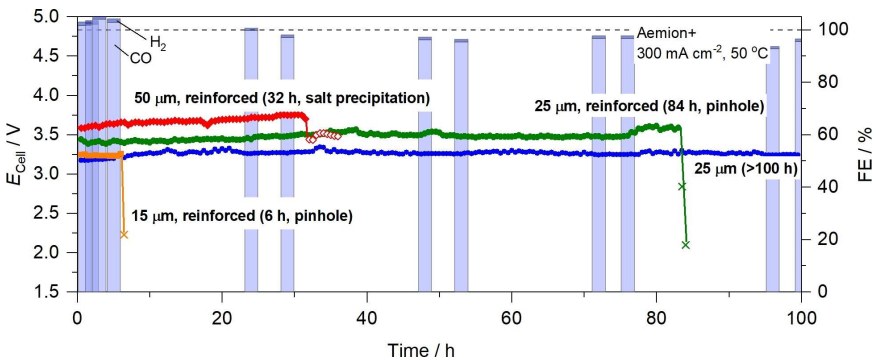

Figure 5. Stability tests for various Aemion+ membranes (AF2-CLE8-X and AH2-INN8-25-X) used in a CO_2E cell operating at 300 mA cm^{-2} with a cell temperature of 50 °C. E_{Cell} is shown for all AEMs (symbols) alongside the FE (bars) for the 25 μm Aemion+ membrane. 10 mM $KHCO_3$ (1.5 L, heated to 50 °C) was recirculated at a flow rate of 10 mL min^{-1}. Humidified CO_2 (dew point = 50 °C) was supplied to the cathode with a flow rate of 30 mL min^{-1}. Ag cathode and IrO_2 anodes (Dioxide Materials) were cut to exactly 5 cm^2. The cause for discontinuing the test is described in brackets.

shown in Figure S14 demonstrates changes to the HFR, where an increase up to 48 h is followed by a decrease until the end of the experiment. The decrease in HFR towards the end of the experiment is similar to that observed for Aemion (100 mA cm^{-2}, RT) in Figure 1e and non-reinforced Aemion+ (300 mA cm^{-2}, RT) in Figure S13. Coinciding with the decrease in total FE and E_{Cell}, it is predicted that eventual edge failure similar to the experiment at room temperature would have occurred if the cell had been left for longer times. This leads to the conclusion that the reinforcement remains pivotal for enabling the stable use of thin AEMs which exhibit lower E_{Cell}.

It is therefore paramount to better understand and alleviate the pinholes that form with the reinforced AEM. Thicker (reinforced) Aemion+ membranes were therefore examined. Figure 5 shows that a slight increase in the thickness of the reinforced Aemion+ to 25 μm sustained a high FE (average of 98%) and relatively stable E_{Cell} of 3.48 V for 84 h, before a sudden drop in voltage occurred, indicating pinhole formation. Figure S14 shows that the impedance response up until the point of cell failure remained consistent and so failure of the membrane is highly localized, yet bulk conductivity is little affected. The higher cell voltage compared to the non-reinforced AEM of equal thickness is likely due to the previously reported reduction in water permeability of Aemion+ when a reinforcement is used,[58] which might also explain the why a pinhole was not observed for the non-reinforced membrane.

Figure 5 shows that a 50 μm, reinforced AEM achieved an initial E_{Cell} of 3.59 V. (the FE_{CO} was initially around 90%). However, salt precipitation at the CO_2 inlet of the flow field plate, shown in Figure S15a, blocked the gas supply after 31 h. As shown in Figure S15b, the cell performance was recoverable by disassembling the cell and washing the precipitated salt from the cathode, but blockage of the cathode flow field plate re-occurred 13 h after re-initiating a current density of 300 mA cm^{-2}. With an increased thickness, the rate of diffusion of dissolved K_2CO_3 to the anode will be reduced, leading to an imbalanced build up and saturation of salts at the cathode.[43]

Combined, these results indicate that for electrolyzer stability, there is an optimum thickness of the membrane that is thin enough to provide sufficient water permeation to the cathode and salt removal back to the anode, but not so thin as to be susceptible to mechanical failure. A reinforcement avoids mechanical failure at the edges, but the effects on the transport properties of the AEM need to be taken into account.

Synergistic effects of the cathode composition and membrane stability

Modelling[71] and neutron imaging of both CO_2E and AEM-WE systems[72,73] have both shown localized dehydration of the AEM at the interface with the catalyst layer due to high rates of water consumption at high current densities. It is therefore hypothesized that increasing the current distribution within the cathode might alleviate localized dehydration at the interface. To examine this, four GDEs with different Ag loading were prepared, using Aemion+ (AP2-INN8-00-X) binder in the catalyst layers at 5 wt%. Higher loadings of ionomer were found to result in higher cell voltages and lower FE_{CO}, indicative of increased mass transport limitations for CO_2 (Figure S16). Figure 6a shows a clear trend between the cell lifetime and the Ag loading at the cathode when using a 15 μm reinforced Aemion+ membrane. A catalyst loading of 0.1 or 0.2 mg$_{Ag}$ cm^{-2} resulted in a steep rise in E_{Cell} within 15 min and 3 h, respectively. This was similar to what was observed for the 25 μm, Aemion membrane at 300 mA cm^{-2}. The two GDEs with higher loadings exhibited progressively smaller rises in E_{Cell} followed by a decay and finally a sudden drop. This occurred at around 18 h and 59 h for the 1 mg$_{Ag}$ cm^{-2} and 2 mg$_{Ag}$ cm^{-2} GDEs, respectively. FE of the cathode gases is also shown in Figure 6a for the 2 mg$_{Ag}$ cm^{-2} GDE, which exhibited high selectivity towards CO, compared to H_2. The drop in total FE for the period 48–53 h illustrates that the drop in cell voltage is attributable to an increase in gas crossover resulting in depolarization of the cell, with a sudden drop in E_{Cell} due to pinhole formation.

Figure 6b shows the initial E_{Cell} (for 5 h) and the FE_{CO} (at 1 h) for the tested GDEs. It is interesting to note that the initial E_{Cell} of 3.50 V for the 0.1 mg$_{Ag}$ cm^{-2} GDE was only reduced to 3.41 V

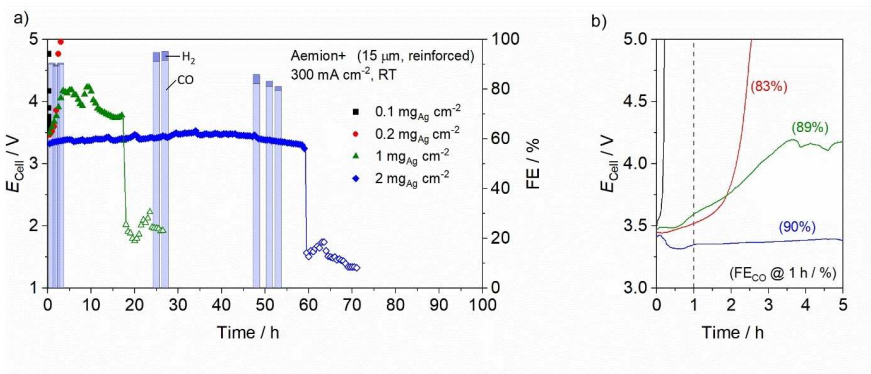

Figure 6. Stability tests for cathode GDEs with various Ag loadings used in a CO_2E cell operating at room temperature with a current density of 300 mA cm^{-2}. a) E_{Cell} is shown for all GDEs alongside the FE for the 2 mg$_{Ag}$ cm^{-2} loading. b) E_{Cell} for the first 5 h is shown with the FE_{CO} after 1 h operation. 10 mM $KHCO_3$ (500 mL) was recirculated at a flow rate of 10 mL min^{-1}. Humidified CO_2 was supplied to the cathode with a flow rate of 30 mL min^{-1}. IrO_2 anodes (Dioxide Materials) and the cathode GDEs were cut to exactly 5 cm^2. Aemion+ (15 μm, reinforced) was used for all tests.

with the 20-fold increase in loading to 2 $mg_{Ag}\,cm^{-2}$. Hansen *et al.*, recently showed that there is a significant ohmic resistance at the cathode|membrane interface when using GDEs and so here, the impact of catalyst loading on the overpotential for the CO_2R might be less significant than if this resistance was reduced by the fabrication of catalyst coated membranes, for example.[74] The lower FE_{CO} of 83% for the 0.1 $mg_{Ag}\,cm^{-2}$ GDE is due to a lower FE_{total} ($FE_{CO}+FE_{H2}$) of 85% compared to 91% for the 1 $mg_{Ag}\,cm^{-2}$ and 2 $mg_{Ag}\,cm^{-2}$ GDEs, indicative of increased gas crossover due to membrane degradation.

These results demonstrate a clear synergy between the cathode surface area and AEM degradation, supporting the hypothesis that pinhole formation is due to localized dehydration at the GDE|AEM interface. Ex situ double layer capacitance measurements were carried out and as shown in Figure S17, a capacitance increase of 0.439 $\mu F\,mg_{Ag}^{-1}$ was measured. Assuming a standard capacitance of 25 $\mu F\,cm_{Ag}^{-2}$,[75] this equates to an ECSA of just 0.002 $m^2\,g_{Ag}^{-1}$. Considering that the development of Pt/C catalysts for PEMFCs has rendered ECSA $>80\,m^2\,g_{Pt}^{-1}$ frequently achievable, this result suggests significant room for increasing the catalytically active surface area of these electrodes. It is therefore anticipated that while catalyst and catalyst layer development will help to reduce the overall cell voltage of these systems, such efforts could also increase the stability of the membrane in CO_2 electrolyzers operating at high current densities.

Conclusions

It has been shown that when using milder anolyte solutions (10 mM $KHCO_3$ vs. 1 M KOH), CO_2E can operate with high stability (>100 h at 100 $mA\,cm^{-2}$) by avoiding issues such as anolyte neutralization and rapid salt precipitation. However, the stability enhancements come with a significant penalty to the energetic efficiency of the cell and an increase in the sensitivity of the cell voltage to changes in membrane properties. EIS analysis comparing Aemion with Aemion+ shows that the AEM affects the charge transfer and mass transport resistance elements to a greater extent than the ohmic resistances of the cell. Ex situ permselectivity measurements shows that the reduction in charge transfer resistance and subsequent 0.19 V decrease in the cell voltage at 200 $mA\,cm^{-2}$, when using Aemion+ instead of Aemion, can not just be attributed to increases in water permeability, but are also likely to be a result of an increase in co-ion leakage through the AEM.

These changes to membrane properties were found to also correlate with the increased voltage stability at higher current densities (300 $mA\,cm^{-2}$). However, it was found that edge failure of the highly swollen AEMs limits future applicability. Edge failure was shown to be mitigated through the use of a reinforcement, which decreased the volumetric swelling of the AEM to 64% of the value of the non-reinforced sample, and also enabled the use of thinner AEMs. While thinner AEMs are shown to be one strategy for decreasing E_{Cell} further (to 3.17 V at 200 $mA\,cm^{-2}$) through an increase in the water permeance, thin AEMs were found to have an increased propensity for pinhole formation and catastrophic cell failure. Thicker AEMs on the other hand reinforced issues with salt precipitation. By varying the loading of Ag on the cathode GDEs, a synergy between electrochemically active surface area and pinhole formation is shown. This result suggests that localized dehydration at the cathode|AEM interface is the probable cause of pinhole formation and can be mitigated with developments of the cathode catalyst layer, in addition to membrane properties.

In order to fully elucidate how membrane properties affect electrolyzer performance, a comprehensive study combining electrolyzer modelling with high throughput characterization of membrane properties such as water permeability, permselectivity, dimensional swelling, conductivity and thickness, all in the different counter-ion forms present during electrolysis (OH^-/CO_3^{2-}/HCO_3^-) would be beneficial. CO_2R towards higher order carbons will also need to consider properties such as neutral product crossover and the stability of CO_2E in the presence of alcohols. Finally, a greater understanding on the effect of cathode properties such as the electrochemically active surface area and current distribution on membrane stability is also critical. It is the hope of the authors that this investigation provides insight into such efforts.

Experimental Section

Materials

All H_2O was deionized (DI) to 18.2 MΩ cm with a Milli-Q water purification system. KOH pellets, $KHCO_3$, Ag nanoparticles (< 100 nm) were all obtained from Sigma-Aldrich and used as received. NaCl was obtained from Fisher-Scientific. Sigracet 22BB GDLs were purchased from Ion-Power. Dimethyl sulfoxide-D6 (D, 99.9%, DMSO-d6) was purchased from Cambridge Isotope Laboratories. Ag/AgCl wire electrodes were prepared in-house according to our previously published method.[61] The IrO_2 anodes, Ag cathodes, PTFE gaskets, Ti and stainless-steel flow field plates were all purchased from Dioxide Materials. Aemion and Aemion+ materials were provided by Ionomr Innovations Inc.

Electrode fabrication

Catalyst inks had a composition of 1 wt% solids in a 1:3 (*v*/*v*) mixture of H_2O/MeOH. Ag nanoparticles were firstly added to a vial, followed by the required amount of DI water. The required aliquot of MeOH, followed by 2 wt% of Aemion+ solvated in MeOH were then added to achieve the desired ink composition. The catalyst ink was then sonicated in an ultrasonic bath (Branson) filled with ice for 1 h. The catalyst ink was then immediately hand sprayed onto a piece of Sigracet 22BB GDL heated to 80 °C by a hot plate. 1 mL of the catalyst ink was sprayed at a time with the remaining ink under continuous ultra-sonication. The final loadings were measured by mass balance.

Mechanical strength tests

Elongation-to-break tests on polymer membranes in their bicarbonate (HCO_3^-) form were conducted using a single column Instron 3344 Series. Ion-exchanged membranes stored in Milli-pore water were prepared by drying them between paper towels and an

added weight for at least 2 days under ambient conditions. For tensile testing, membranes were cut into rectangular samples of 4x1 cm ($l \times w$). Sample thicknesses were recorded along the entire sample length and averaged. Tests were conducted under ambient conditions, with a temperature of 20 °C and an RH that varied between 30–35 %. The applied elongation rate was 5 mm min^{-1}. Results for Young's modulus, yield strength, and elongation-at-break are reported as averages over at least three samples.

Water uptake

Water uptake of polymer membranes in their bicarbonate (HCO_3^-) form was measured gravimetrically. To determine the samples' wet weight, ion-exchanged membranes stored in Millipore water at room temperature for at least 3 days were dabbed dry using Kimwipes™ to remove any water on the surface of the membrane, and quickly weighed. After measurement, membrane pieces were rehydrated in water and the weighing was repeated at least three times for each sample to ensure reliability. Sample dry weight was determined afterwards by drying membranes for at least 24 h in a vacuum oven at 80 °C. For each membrane type, three samples were treated and weighed separately. Water uptake (WU, $g_{H_2O}\, g_{dry}^{-1}$) was calculated using the samples' wet (w_{wet}) and dry (w_{dry}) weight according to Equation (1):

$$\mathrm{WU} = \frac{w_{\mathrm{wet}} - w_{\mathrm{dry}}}{w_{\mathrm{dry}}} \tag{1}$$

Permselectivity measurements

Our previously reported membrane potential based static method was employed to measure the counter-ion transport numbers and permselectivity of the AEMs.[61] The membrane potential was measured using a two-compartment H-type acrylic cell with 15 mL of volume in each compartment. Two Ag/AgCl coated wire reference electrodes were used at a distance of 3 mm from the membrane sample holder in both compartments to measure the membrane potential. Wire electrodes were used to avoid additional junction potentials from the reference electrode.[76] The two compartments, separated by AEM samples were clamped together. A dual channel peristaltic pump (BT100-1 L–B, DG-2-B, Langer Instruments Corp., USA) was used to circulate 0.5 M and 0.1 M NaCl solution into the compartments at a rate of 23 mL min^{-1}. To ensure that the solutions on either side of the AEMs were well mixed during the measurement, magnetic stirrers were positioned on both sides of the cell for rigorous mechanical stirring. All experiments were carried out on three membrane samples for each type and at an ambient temperature of 20 ± 0.3 °C. A digital multimeter was used to measure the potential (E_{meas}) across the two reference electrodes, and was recorded after approximately 30–60 min, once stabilized. The membrane potential (E_{mem}) was obtained by Equation (2) where E_{meas} was corrected for the ideal potential difference of Ag/AgCl wire reference electrodes in the two solutions at 20 °C ($\Delta E_{Ag/AgCl,ideal} = -37.24$ mV, Equation (3))[–61,76,77] and the average off-set potential between the two reference electrodes measured in both 0.1 and 0.5 M NaCl solutions, calculated by Equation (4).

$$E_{\mathrm{mem}} = E_{\mathrm{meas}} - \Delta E_{\mathrm{Ag/AgCl,\ ideal}} - E_{\mathrm{offset}} \tag{2}$$

$$\begin{aligned} \Delta E_{\mathrm{Ag/AgCl,ideal}} &= -\frac{RT}{zF}\ln\left(\frac{a_{\mathrm{Cl}}^{\mathrm{H,\ 0.5\ M}}}{a_{\mathrm{Cl}}^{\mathrm{L,\ 0.1\ M}}}\right) \\ &= -\frac{RT}{F}\ln\left(\frac{C_{\mathrm{Cl}}^{\mathrm{H,\ 0.5\ M}}\gamma_{\mathrm{Cl}}^{\mathrm{H,\ 0.5\ M}}}{C_{\mathrm{Cl}}^{\mathrm{L,\ 0.1\ M}}\gamma_{\mathrm{Cl}}^{\mathrm{L,\ 0.1\ M}}}\right) \end{aligned} \tag{3}$$

$$E_{offset} = \frac{\Delta E_{0.5\ M} + \Delta E_{0.1\ M}}{2} \tag{4}$$

R is the ideal gas constant (8.314 J mol^{-1} K^{-1}), F is the Faraday constant (96485 C mol^{-1}), T is the absolute temperature [K], z is the absolute charge of the anion, $a_{\mathrm{Cl}}^{\mathrm{H,\ 0.5\ M}}$ and $a_{\mathrm{Cl}}^{\mathrm{L,\ 0.1\ M}}$ are the mean activity values of Cl^- in the high concentration (0.5 M) and low concentration (0.1 M) NaCl solutions, respectively. $c_{\mathrm{Cl}}^{\mathrm{H,\ 0.5\ M}}$ and $c_{\mathrm{Cl}}^{\mathrm{L,\ 0.1\ M}}$ are the respective concentrations while $\gamma_{\mathrm{Cl}}^{\mathrm{H,\ 0.5\ M}}$ and $\gamma_{\mathrm{Cl}}^{\mathrm{L,\ 0.1\ M}}$ are the activity coefficients, taken as 0.680 and 0.778 (at 20 °C), respectively.[78]

By measuring E_{mem}, the counter-ion transport number through the membrane phase ($t_{\mathrm{Counter-ion}}^{\mathrm{mem}}$) were then calculated using Equation (6).

$$E_{\mathrm{mem}} = \left(2t_{\mathrm{Counter-ion}}^{\mathrm{mem}} - 1\right)\frac{RT}{zF}\ln\left(\frac{a_{\mathrm{Cl}}^{\mathrm{H,\ 0.5\ M}}}{a_{\mathrm{Cl,}}^{\mathrm{L,\ 0.1\ M}}}\right) \tag{5}$$

$$t_{\mathrm{Counter-ion}}^{\mathrm{mem}} = \frac{\left[E_{\mathrm{mem}} / \frac{RT}{F}\ln\left(\frac{a_{\mathrm{Cl}}^{\mathrm{H,\ 0.5\ M}}}{a_{\mathrm{Cl,}}^{\mathrm{L,\ 0.1\ M}}}\right)\right] + 1}{2} \tag{6}$$

The apparent permselectivity (α) values were finally calculated using Equation (7).

$$\alpha = \frac{t_{\mathrm{Counter-ion}}^{\mathrm{mem}} - t_{\mathrm{Counter-ion}}^{\mathrm{sol}}}{t_{\mathrm{Co-ion}}^{\mathrm{sol}}} \tag{7}$$

$t_{\mathrm{Counter-ion}}^{\mathrm{sol}}$ is the counter-ion transport number ($t_{Na^+} = 0.395$) and $t_{\mathrm{Co-ion}}^{\mathrm{sol}}$ is the co-ion transport number ($t_{Cl^-} = 0.605$) in the solution phase surrounding the AEM.[61]

CO_2 electrolysis

CO_2E was performed in a cell of 5 cm^2 active area, utilizing titanium and stainless-steel flow field plates with single serpentine flow channel at the anode and cathode, respectively. Unless specified, IrO_x anodes (Dioxide Materials) and Ag cathodes (Dioxide Materials) were used with 270 µm PTFE gaskets on both sides. The electrodes were cut to 5.0 ± 0.3 cm^2 prior to assembly. After activation in 3 M KOH for 2 days (exchanging the solution once), AEMs were stored in 0.5 M KOH no longer than 14 days. For assembly, AEMs were taken from the 0.5 M KOH solution and placed in between electrodes. The cell was compressed to 1.13 N m using a torque screwdriver.

10 mM $KHCO_3$ (500 mL) was then recirculated through the anode at a flow rate of 10 mL min^{-1}. Humidified CO_2 was supplied to the cell by a water bubbler at a flow rate of 30 mL min^{-1}, controlled by a mass flow controller calibrated for CO_2 (Alicat, MCW-200SCCM–D/CM). For experiments at 50 °C, a humidifier and anolyte reservoir were heated by three heating probes and one thermocouple inserted directly into the solutions. These were protected by a PTFE coating. The CO_2 inlet from the bubbler was insulated and the cell was heated with two 50 W/110 V heating pads (Dioxide Materials).

The electrochemical cell, gas humidifier and anolyte reservoir were all heated to 50 °C. Downstream of the electrolyzer on the cathode side, a desiccant was installed followed by a mass flow meter (Alicat, MW-200SCCM–D/CM). An on-line Agilent 990 micro-GC system with 1 m COx column was used for analysis of the gas mixtures pre-calibrated with three separate mixtures of H_2 and CO in a balance of N_2 (NorLab). Further details including the calculation for the FE of the product gases are provided in our previous publication.[26] For electrochemical characterization, a Tektronix PWS4205 Programmable DC Power Supply (0–20 V, 5 A) with Advanced Measurements Inc. software was used. All (Galvano) electrochemical impedance spectroscopy (EIS) was measured with a Solartron SI1287 Electrochemical Interface with SI2160 Impedance/Gain Analyzer in the frequency range 10 kHz to 0.1 Hz with an amplitude of 5% the DC current. All resistance values in the manuscript were extracted using the equivalent circuit model shown as Figure S2.

To obtain consistent electrolyzer performances, an activation procedure was implemented. After assembly, the electrolyzer was quickly ramped up to 300 mA cm^{-2} with a voltage cap of 5 V to prevent significant corrosion of the carbon-based porous transport layer at the anode. The cell was left to operate until a stable voltage was reached before analyzing the gaseous products from the cathode compartment by gas chromatography (GC) and performing EIS. An example of the activation procedure is shown in Figure S3. Subsequent current densities of 200, 100, 50 and 25 mA cm^{-2} were applied with at least 15 min equilibration time before EIS and recording the final cell voltage (E_{Cell}). For the stability measurements, it was found that pre-wetting the cathodes on-top of 1 M KOH solution significantly decreased the time required to activate the cell. A current density of 100 or 300 mA cm^{-2} was applied and the cell voltage (recorded every 1 min) was averaged every 30 min. GC and EIS were conducted periodically.

AEMs were exchanged back to the chloride form immediately after cell disassembly. ^{1}H nuclear magnetic resonance spectroscopy (NMR) was performed on select AEMs after the stability test with a 400 MHz Bruker AVANCE III running IconNMR under TopSpin 2.1. NMR spectra were calibrated at the solvent peaks for DMSO-d6 at 2.50 ppm. Chemical stability was assessed by comparing integrations between the aromatic region (8.1–7.3 ppm) which integrate for 18 protons and the aliphatic region and more particularly the region between (3.79–3.4 ppm) which should integrate ideally for 12 protons. This was conducted for the membranes before and after the stability test, where any reduction in the aliphatic region would indicate chemical degradation by defunctionalization.

Acknowledgements

This work was funded by the National Research Council of Canada's Materials for Clean Fuels Challenge Program (Collaborative Research agreement: MCF-103-1). The authors would like to acknowledge Ionomr Innovations Inc., who, as part of this grant, supplied Aemion and Aemion + materials for the project. The authors would also like to thank Ruoxi Qiao, Harry Riley and Faezeh Habibzadeh from the National Research Council of Canada for assistance and helpful discussions during this project.

Conflict of Interests

Steven Holdcroft is a co-founder and scientific advisor of Ionomr Innovations Inc, Vancouver, supplier of Aemion and Aemion + membranes used in this work.

Data Availability Statement

The data that support the findings of this study are available from the corresponding author upon reasonable request.

Keywords: anion exchange membrane · CO2 electrolysis · stability · permselectivity · Aemion

[1] Y. Shi, C. Eze, B. Xiong, W. He, H. Zhang, T. M. Lim, A. Ukil, J. Zhao, *Appl. Energy* **2019**, *238*, 202–224.
[2] D. Chen, M. A. Hickner, E. Agar, E. C. Kumbur, *Electrochem. Commun.* **2013**, *26*, 37–40.
[3] D. R. Dekel, *J. Power Sources* **2018**, *375*, 158–169.
[4] Z. F. Pan, L. An, T. S. Zhao, Z. K. Tang, *Prog. Energy Combust. Sci.* **2018**, *66*, 141–175.
[5] W. Mustain, M. Chatenet, M. Page, Y. S. Kim, *Energy Environ. Sci.* **2020**, *13*, 2805–2838.
[6] N. Du, C. Roy, R. Peach, M. Turnbull, S. Thiele, C. Bock, *Chem. Rev.* **2022**, *122*, 11830–11895.
[7] D. Li, A. R. Motz, C. Bae, C. Fujimoto, G. Yang, F.-Y. Zhang, K. E. Ayers, Y. S. Kim, *Energy Environ. Sci.* **2021**, *14*, 3393–3419.
[8] I. Vincent, D. Bessarabov, *Renewable Sustainable Energy Rev.* **2018**, *81*, 1690–1704.
[9] D. Henkensmeier, M. Najibah, C. Harms, J. Žitka, J. Hnát, K. Bouzek, *J. Electrochem. Energy Convers. Storage* **2021**, *18*, 024001.
[10] D. Salvatore, C. Gabardo, A. Reyes, C. O'Brien, S. Holdcroft, P. Pintauro, B. Bahar, M. Hickner, C. Bae, D. Sinton, E. Sargent, C. Berlinguette, *Nat. Energy* **2021**, *6*, 339–348.
[11] E. W. Lees, B. A. W. Mowbray, F. G. L. Parlane, C. P. Berlinguette, *Nat. Rev. Mater.* **2022**, *7*, 55–64.
[12] H. Jung, S. Choung, J. W. Han, *Nanoscale Adv.* **2021**, *3*, 6797–6826.
[13] M. Schalenbach, G. Tjarks, M. Carmo, W. Lueke, M. Mueller, D. Stolten, *J. Electrochem. Soc.* **2016**, *163*, F3197–F3208.
[14] H. A. Firouzjaie, W. E. Mustain, *ACS Catal.* **2020**, *10*, 225–234.
[15] L. Giordano, B. Han, M. Risch, W. T. Hong, R. R. Rao, K. A. Stoerzinger, Y. Shao-Horn, *Catal. Today* **2016**, *262*, 2–10.
[16] T. Cheng, L. Wang, B. V. Merinov, W. A. Goddard III, *J. Am. Chem. Soc.* **2018**, *140*, 7787–7790.
[17] J. Durst, A. Siebel, C. Simon, F. Hasché, J. Herranz, H. A. Gasteiger, *Energy Environ. Sci.* **2014**, *7*, 2255–2260.
[18] A. Ozden, F. P. García de Arquer, J. E. Huang, J. Wicks, J. Sisler, R. K. Miao, C. P. O'Brien, G. Lee, X. Wang, A. H. Ip, E. H. Sargent, D. Sinton, *Nat. Sustain.* **2022**, *5*, 563–573.
[19] J. E. Huang, F. Li, A. Ozden, A. S. Rasouli, F. P. García de Arquer, S. Liu, S. Zhang, M. Luo, X. Wang, Y. Lum, Y. Xu, K. Bertens, R. K. Miao, C.-T. Dinh, D. Sinton, E. H. Sargent, *Science* **2021**, *372*, 1074–1078.
[20] F. Liang, K. Zhang, L. Zhang, Y. Zhang, Y. Lei, X. Sun, *Small* **2021**, *17*, 2100323.
[21] S. Garg, M. Li, A. Z. Weber, L. Ge, L. Li, V. Rudolph, G. Wang, T. E. Rufford, *J. Mater. Chem. A* **2020**, *8*, 1511–1544.
[22] H. Shin, K. U. Hansen, F. Jiao, *Nat. Sustain.* **2021**, *4*, 911–919.
[23] J. A. Rabinowitz, M. W. Kanan, *Nat. Commun.* **2020**, *11*, 10–12.
[24] M. Ma, S. Kim, I. Chorkendorff, B. Seger, *Chem. Sci.* **2020**, *11*, 8854–8861.
[25] M. Ma, E. L. Clark, K. T. Therkildsen, S. Dalsgaard, I. Chorkendorff, B. Seger, *Energy Environ. Sci.* **2020**, *13*, 977–985.
[26] P. Mardle, S. Cassegrain, F. Habibzadeh, Z. Shi, S. Holdcroft, *J. Phys. Chem. C* **2021**, *125*, 25446–25454.
[27] H. Haspel, J. Gascon, *ACS Appl. Energ. Mater.* **2021**, *4*, 8506–8516.
[28] G. O. Larrazábal, P. Strøm-Hansen, J. P. Heli, K. Zeiter, K. T. Therkildsen, I. Chorkendorff, B. Seger, *ACS Appl. Mater. Interfaces* **2019**, *11*, 41281–41288.

[29] J. Sisler, S. Khan, A. H. Ip, M. W. Schreiber, S. A. Jaffer, E. R. Bobicki, C.-T. Dinh, E. H. Sargent, *ACS Energy Lett.* **2021**, *6*, 997–1002.
[30] T. Alerte, J. P. Edwards, C. M. Gabardo, C. P. O'Brien, A. Gaona, J. Wicks, A. Obradović, A. Sarkar, S. A. Jaffer, H. L. MacLean, D. Sinton, E. H. Sargent, *ACS Energy Lett.* **2021**, *6*, 4405–4412.
[31] A. Ozden, Y. Wang, F. Li, M. Luo, J. Sisler, A. Thevenon, A. Rosas-Hernández, T. Burdyny, Y. Lum, H. Yadegari, T. Agapie, J. C. Peters, E. H. Sargent, D. Sinton, *Joule* **2021**, *5*, 706–719.
[32] X. Wang, P. Ou, A. Ozden, S.-F. Hung, J. Tam, C. M. Gabardo, J. Y. Howe, J. Sisler, K. Bertens, F. P. García de Arquer, R. K. Miao, C. P. O'Brien, Z. Wang, J. Abed, A. S. Rasouli, M. Sun, A. H. Ip, D. Sinton, E. H. Sargent, *Nat. Energy* **2022**, *7*, 170–176.
[33] M. Jouny, G. S. Hutchings, F. Jiao, *Nat. Catal.* **2019**, *2*, 1062–1070.
[34] Y. C. Li, D. Zhou, Z. Yan, R. H. Gonçalves, D. A. Salvatore, C. P. Berlinguette, T. E. Mallouk, *ACS Energy Lett.* **2016**, *1*, 1149–1153.
[35] D. A. Salvatore, D. M. Weekes, J. He, K. E. Dettelbach, Y. C. Li, T. E. Mallouk, C. P. Berlinguette, *ACS Energy Lett.* **2018**, *3*, 149–154.
[36] T. Li, E. W. Lees, M. Goldman, D. A. Salvatore, D. M. Weekes, C. P. Berlinguette, *Joule* **2019**, *3*, 1487–1497.
[37] E. W. Lees, M. Goldman, A. G. Fink, D. J. Dvorak, D. A. Salvatore, Z. Zhang, N. W. X. Loo, C. P. Berlinguette, *ACS Energy Lett.* **2020**, *5*, 2165–2173.
[38] L.-C. Weng, A. T. Bell, A. Z. Weber, *Energy Environ. Sci.* **2019**, *12*, 1950–1968.
[39] D. G. Wheeler, B. A. W. Mowbray, A. Reyes, F. Habibzadeh, J. He, C. P. Berlinguette, *Energy Environ. Sci.* **2020**, *13*, 5126–5134.
[40] B. De Mot, M. Ramdin, J. Hereijgers, T. J. H. Vlugt, T. Breugelmans, *ChemElectroChem* **2020**, *7*, 3839–3843.
[41] S. Verma, Y. Hamasaki, C. Kim, W. Huang, S. Lu, H.-R. M. Jhong, A. A. Gewirth, T. Fujigaya, N. Nakashima, P. J. A. Kenis, *ACS Energy Lett.* **2018**, *3*, 193–198.
[42] B. Endrödi, E. Kecsenovity, A. Samu, F. Darvas, R. V. Jones, V. Török, A. Danyi, C. Janáky, *ACS Energy Lett.* **2019**, *4*, 1770–1777.
[43] Y. Xu, J. P. Edwards, S. Liu, R. K. Miao, J. E. Huang, C. M. Gabardo, C. P. O'Brien, J. Li, E. H. Sargent, D. Sinton, *ACS Energy Lett.* **2021**, *6*, 809–815.
[44] B. Endrődi, A. Samu, E. Kecsenovity, T. Halmágyi, D. Sebők, C. Janáky, *Nat. Energy* **2021**, *6*, 439–448.
[45] M. R. Thorson, K. I. Siil, P. J. A. Kenis, *J. Electrochem. Soc.* **2013**, *160*, F69–F74.
[46] S. Popović, M. Smiljanić, P. Jovanovič, J. Vavra, R. Buonsanti, N. Hodnik, *Angew. Chem. Int. Ed.* **2020**, *59*, 14736–14746.
[47] A. A. Samu, A. Kormányos, E. Kecsenovity, N. Szilágyi, B. Endrődi, C. Janáky, *ACS Energy Lett.* **2022**, *7*, 1859–1861.
[48] B. Endrődi, E. Kecsenovity, A. Samu, T. Halmágyi, S. Rojas-Carbonell, L. Wang, Y. Yan, C. Janáky, *Energy Environ. Sci.* **2020**, *13*, 4098–4105.
[49] S. Verma, X. Lu, S. Ma, R. I. Masel, P. J. A. Kenis, *Phys. Chem. Chem. Phys.* **2016**, *18*, 7075–7084.
[50] J. Resasco, L. D. Chen, E. Clark, C. Tsai, C. Hahn, T. F. Jaramillo, K. Chan, A. T. Bell, *J. Am. Chem. Soc.* **2017**, *139*, 11277–11287.
[51] S. Ringe, E. L. Clark, J. Resasco, A. Walton, B. Seger, A. T. Bell, K. Chan, *Energy Environ. Sci.* **2019**, *12*, 3001–3014.
[52] A. Kiessling, J. C. Fornaciari, G. Anderson, X. Peng, A. Gerstmayr, M. R. Gerhardt, S. McKinney, A. Serov, Y. S. Kim, B. Zulevi, A. Z. Weber, N. Danilovic, *J. Electrochem. Soc.* **2021**, *168*, 084512.
[53] J. Qiao, Y. Liu, F. Hong, J. Zhang, *Chem. Soc. Rev.* **2014**, *43*, 631–675.
[54] R. B. McCleskey, *J. Chem. Eng. Data* **2011**, *56*, 317–327.
[55] R. J. Gilliam, J. W. Graydon, D. W. Kirk, S. J. Thorpe, *Int. J. Hydrogen Energy* **2007**, *32*, 359–364.
[56] N. Ziv, D. R. Dekel, *Electrochem. Commun.* **2018**, *88*, 109–113.
[57] A. Reyes, R. P. Jansonius, B. A. W. Mowbray, Y. Cao, D. G. Wheeler, J. Chau, D. J. Dvorak, C. P. Berlinguette, *ACS Energy Lett.* **2020**, *5*, 1612–1618.
[58] Q. Wei, X. Cao, P. Veh, A. Konovalova, P. Mardle, P. Overton, S. Cassegrain, S. Vierrath, M. Breitwieser, S. Holdcroft, *Sustain. Energy Fuels* **2022**, *6*, 3551–3564.
[59] D. Salvatore, C. P. Berlinguette, *ACS Energy Lett.* **2020**, *5*, 215–220.
[60] Q. Xu, S. Z. Oener, G. Lindquist, H. Jiang, C. Li, S. W. Boettcher, *ACS Energy Lett.* **2021**, *6*, 305–312.
[61] A. S. Gangrade, S. Cassegrain, P. Chandra Ghosh, S. Holdcroft, *J. Membr. Sci.* **2022**, *641*, 119917–119928.
[62] G. M. Geise, H. J. Cassady, D. R. Paul, B. E. Logan, M. A. Hickner, *Phys. Chem. Chem. Phys.* **2014**, *16*, 21673–21681.
[63] T. Sata, Ion Exchange Membranes: Preparation, Characterization, Modification and Application, Royal Society Of Chemistry, **2007**.
[64] Z. Liu, H. Yang, R. Kutz, R. I. Masel, *J. Electrochem. Soc.* **2018**, *165*, J3371–J3377.
[65] W. H. Lee, Y. J. Ko, Y. Choi, S. Y. Lee, C. H. Choi, Y. J. Hwang, B. K. Min, P. Strasser, H.-S. Oh, *Nano Energy* **2020**, *76*, 105030.
[66] Y. Wu, S. Garg, M. Li, M. N. Idros, Z. Li, R. Lin, J. Chen, G. Wang, T. E. Rufford, *J. Power Sources* **2022**, *522*, 230998.
[67] M. E. Leonard, L. E. Clarke, A. Forner-Cuenca, S. M. Brown, F. R. Brushett, *ChemSusChem* **2020**, *13*, 400–412.
[68] K. Yang, R. Kas, W. A. Smith, T. Burdyny, *ACS Energy Lett.* **2021**, *6*, 33–40.
[69] E. J. Park, C. G. Arges, H. Xu, Y. S. Kim, *ACS Energy Lett.* **2022**, *7*, 3447–3457.
[70] P. Majsztrik, A. Bocarsly, J. Benziger, *J. Phys. Chem. B* **2008**, *112*, 16280–16289.
[71] K. V. Petrov, J. Bui, L. M. Baumgartner, L.-C. Weng, S. Dischinger, D. M. Larson, D. Miller, A. Z. Weber, D. A. Vermaas, *Sustain. Energy Fuels* **2022**, *6*, 5077–5088.
[72] S. Koch, J. Disch, S. K. Kilian, Y. Han, L. Metzler, A. Tengattini, L. Helfen, M. Schulz, M. Breitwieser, S. Vierrath, *RSC Adv.* **2022**, *12*, 20778–20784.
[73] J. Disch, L. Bohn, S. Koch, M. Schulz, Y. Han, A. Tengattini, L. Helfen, M. Breitwieser, S. Vierrath, *Nat. Commun.* **2022**, *13*, 6099.
[74] K. U. Hansen, L. H. Cherniack, F. Jiao, *ACS Energy Lett.* **2022**, 4504–4511.
[75] Y. Yoon, A. S. Hall, Y. Surendranath, *Angew. Chem. Int. Ed.* **2016**, *55*, 15282–15286.
[76] R. S. Kingsbury, S. Flotron, S. Zhu, D. F. Call, O. Coronell, *Environ. Sci. Technol.* **2018**, *52*, 4929–4936.
[77] A. J. Bard, L. R. Faulkner, *Electrochemical Methods Fundamentals and Applications*, John Wiley & Sons, Inc., Hoboken, **2001**.
[78] F. Millero, in *"Activity Coefficients in Electrolyte Solutions"*, CRC Press, **1979**, pp. 63–151.

Manuscript received: December 22, 2022
Revised manuscript received: March 27, 2023
Accepted manuscript online: March 30, 2023
Version of record online: June 13, 2023